

Analysis of Anode Current From a Thermionic Cathode With a 2-D Work Function Distribution

Abhijit Jassem^{ib}, David Chernin^{ib}, John J. Petillo^{ib}, *Senior Member, IEEE*, Y. Y. Lau^{ib}, *Fellow, IEEE*, Aaron Jensen, and Serguei Ovtchinnikov^{ib}

Abstract—A model of a thermionic cathode in a planar diode in which the Poisson and Vlasov equations are solved in 3-D assuming an infinite magnetic field is presented. We explore how 2-D work function variations across the cathode surface may affect the transition between temperature-limited and space-charge-limited flow, commonly known as the “knee” of the Miram curve. We study a variety of work function distributions, both realistic and idealized, and demonstrate how emission from the lowest work function regions dominates the total anode current even when such regions make up a relatively small fraction of cathode area. Our model also illustrates the ability of cathodes to reach the full Child–Langmuir current despite the presence of a sizeable nonemitting region. We find that as the length scale of these work function variations decreases, the Miram knee grows sharper, indicating improved cathode performance.

Index Terms—Cathode, Miram curve, space-charge-limited, temperature-limited, thermionic emission, work function.

I. INTRODUCTION

Thermionic cathodes are commonly used to generate the electron beam that drives a wide variety of vacuum electronic devices, such as traveling wave tubes, klystrons, and magnetrons. For a cathode of work function ϕ operating at temperature T , the emitted current density is given by the Richardson–Dushman law, varying as $\sim T^2 \exp(-\phi/kT)$ where k is Boltzmann’s constant [1]. However, as the cathode temperature is increased, the accumulation of charge due to these ejected electrons may form a potential minimum or virtual cathode that limits further emission [2], [3]. In a simple 1-D model (Fig. 1), the maximum achievable anode current density is set by the Child–Langmuir law [3], [4], which depends only on the diode gap distance d and gap voltage V_a but is independent of any cathode properties such as work function or temperature.

The evolution from the temperature-limited regime to this space-charge-limited regime for a cathode is characterized by its Miram curve, [5] a plot of anode current versus

Manuscript received November 13, 2020; revised December 15, 2020; accepted December 21, 2020. Date of publication January 21, 2021; date of current version March 10, 2021. This work was supported in part by the Defense Advanced Research Projects Agency (DARPA) under Grant HR0011-16-C-0080 and in part by the Air Force Office of Scientific Research (AFOSR) under Grant FA9550-18-1-1503. The review of this article was arranged by Senior Editor C. A. Ekdahl. (*Corresponding author: Y. Y. Lau.*)

Abhijit Jassem and Y. Y. Lau are with the Department of Nuclear Engineering and Radiological Sciences, University of Michigan, Ann Arbor, MI 48109-2104 USA (e-mail: ajassem@umich.edu; yylau@umich.edu).

David Chernin, John J. Petillo, Aaron Jensen, and Serguei Ovtchinnikov are with Leidos Inc., Reston, VA 20190 USA.

Color versions of one or more figures in this article are available at <https://doi.org/10.1109/TPS.2020.3048097>.

Digital Object Identifier 10.1109/TPS.2020.3048097

This work is licensed under a Creative Commons Attribution 4.0 License. For more information, see <https://creativecommons.org/licenses/by/4.0/>

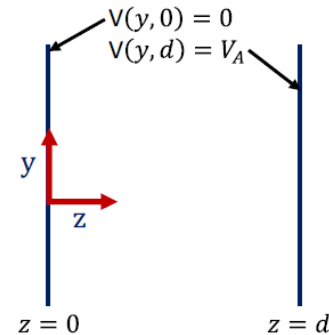


Fig. 1. Planar diode geometry.

cathode temperature, while the transition region is known as the “knee” in the curve. For an ideal 1-D cathode with a uniform work function, the transition is highly abrupt, forming a sharp knee in the Miram curve. However, in experimental curves, this transition occurs much more gradually, resulting in a smooth and rounded knee. The physical reasons behind this discrepancy have not been definitively identified, though one of the factors is conjectured to be the complex surface morphology of the cathode, which introduces spatially varying work function distributions and local field enhancement due to cathode surface roughness. This is an important issue, since thermionic cathodes are almost always operated in the vicinity of the knee for thermal stability and cathode life considerations [6].

There were previous attempts to construct an *ad hoc* “practical work function distribution” (PWFD) directly from the experimental Miram curve [7]. The PWFD usually exhibits a very sharp peak with a very narrow spread of about 0.1 eV in the work function. The PWFD construction is somewhat arbitrary; it does not have a sound physical basis. Chernin *et al.* [8] recently examined the effects of nonuniform cathode emission on the shape of the Miram curve using a novel analytical “1-1/2-D model” and the MICHELLE electron gun code. They considered a cathode whose local work function $\phi(y)$ was allowed to periodically vary in one spatial direction y (Fig. 1), forming work function “stripes.” Electron motion was limited to 1-D by assuming an infinite magnetic field (B) in the z -direction, but the potential was solved for in 2-D, hence the term “1-1/2-D model.” From this work, we reached the following general conclusions:

- 1) Electron motion parallel to the cathode surface does not significantly alter the smoothness or the shape of the Miram knee. That is, the shape of the Miram curve is insensitive to whether we assume $B = 0$ or $B = \infty$.

- 2) Regions of different work functions do not emit independently; they compensate for each other via space-charge forces.
- 3) Most surprisingly, even with a significant nonemitting region, the total anode current obeys the 1-D Child–Langmuir law as if the entire cathode surface were emitting.

The compensatory current effect from (3) echoes the results of Umstadtd and Luginsland [9] who show the formation of current density “wings” on the edges of 2-D emitting patches under space-charge-limited conditions. Like these patches, low work function (highly emissive) regions are not bound by space-charge forces near their boundaries with nonemitting (high work function) regions, allowing them to provide a current density that locally exceeds the 1-D Child Langmuir prediction.

However, the 1-1/2-D model [8] was still not capable of generating the smooth transitions often observed in experimental Miram curves. Nevertheless, some “rounding” of the knees did occur. When the distribution of work function assumed a few discrete values, including a large value (10 eV) to represent a nonemitting stripe, the resulting Miram curve exhibited several distinct slopes. MICHELLE simulations of this striped cathode validated these curves, also showing the distinct slopes [8]. They demonstrated that they were insensitive to changes in applied magnetic field, B , by comparing the simulations with $B = 0$ and $B = 1$ T with analytic results, which assume $B = \infty$. However, if similar spatial variations of the discrete work function distributions were also allowed in the x -direction on the cathode surface (Fig. 1), the 3-D MICHELLE code simulations did show a very smooth and rounded Miram curve, much like those experimentally observed, as we reported in [8]. It is, therefore, of substantial interest to extend the analytic 1-1/2-D model to 2-1/2-D, allowing the local work function $\phi(x, y)$ to vary in both x - and y -directions on the cathode surface. The versatility of the 2-1/2-D code may definitively answer whether the smoothness and roundedness observed in Miram curves is due mainly to the 2-D effects in the work function distribution, or in large part due to the presence of significant nonemitting regions on the cathode. We may also readily examine a variety of idealized and realistic work function patterns to study how various factors, such as the length scale of work function variations and the appearance of a few local “bright spots” corresponding to highly emitting local spots, may impact the shape of the Miram curve. This article reports our findings on these issues.

Section II presents the 2-1/2-D theory. Section III presents the numerical results. Summary and conclusions are given in Section IV.

II. THEORY

The theory largely follows Chernin *et al.* [8], with some minor additions as we extend the treatment to include an additional periodic spatial dimension. We consider a simple planar diode with the grounded cathode located at $z = 0$ and the anode at voltage V_A at $z = d$. An infinite magnetic field $B = B_z = \infty$ is imposed. Allowing for local variations in

the work function $\phi(x, y)$, the emitted current density at the cathode is given by the Richardson–Dushman equation

$$J_{RD}(x, y) = AT^2 e^{-\phi(x, y)/kT} \quad (1)$$

where A is the Richardson coefficient, T is the cathode temperature, and $\phi(x, y)$ is the local work function. Following the approach of Fry and Langmuir [2], [3], we construct the following electron distribution function as a solution of Vlasov’s equation:

$$f(x, y, z, v_z) = \frac{J_{RD}(x, y)}{v_{th}^2} \exp\left(-\frac{mv_z^2/2 + qV(x, y, z)}{kT}\right). \quad (2)$$

Note that the RHS of (2) is functions of constants of motion, x , y , and the total energy of an emitted electron. Poisson’s equation may be written as

$$\nabla^2 V(x, y, z) = \frac{1}{\epsilon_0 v_{th}} \sqrt{\frac{\pi}{2}} J_{RD}(x, y) e^{-qV(x, y, z)/kT} \times \text{erfc}\left(\frac{v_{\min}(x, y, z)}{\sqrt{2}v_{th}}\right) \equiv S(x, y, z) \quad (3)$$

where ϵ_0 is the permittivity of free space, $v_{th} = (kT/m)^{1/2}$ is the thermal velocity, and $v_{\min}(x, y, z)$ is the minimum value of velocity of any electron originating from (x, y) that can reach location z . Expressions for v_{\min} are given in Appendix A of [8].

We consider the work function $\phi(x, y)$ to be periodic functions of (x, y) with periods p_x and p_y . Since the electron motion is limited to 1-D but the potential is solved for in 3-D, we call this the “2-1/2-D model.”

We define N_x and N_y “cell centered” values of x and y , respectively, as

$$x_i = \frac{i + 1/2}{N_x} p_x \quad (4)$$

$$y_j = \frac{j + 1/2}{N_y} p_y \quad (5)$$

for $i = 0, 1, 2, \dots, N_x - 1$ and $j = 0, 1, 2, \dots, N_y - 1$. We then express the potential as a Fourier series

$$V_{ij}(z) = \frac{4}{N_x N_y} \sum_{l=0}^{N_x-1} \sum_{m=0}^{N_y-1} \tilde{V}_{lm}(z) \times \cos\left(\frac{2\pi l x_i}{p_x}\right) \cos\left(\frac{2\pi m y_j}{p_y}\right) \quad (6)$$

for $l = 0, 1, 2, \dots, N_x - 1$ and $m = 0, 1, 2, \dots, N_y - 1$ where the prime marks on the summations denote that the $l = 0, m = 0$ terms each have an additional factor of 1/2. We discretize the second derivatives with respect to x and y in (3) and reduce the 3-D problem to a set of coupled 1-D problems to find that $\tilde{V}_{lm}(z)$ satisfies

$$\frac{d^2}{dz^2} \tilde{V}_{lm}(z) - 2 \left[\frac{1 - \cos \theta_l}{\Delta x^2} + \frac{1 - \cos \theta_m}{\Delta y^2} \right] \tilde{V}_{lm}(z) = \tilde{S}_{lm}(z) \quad (7)$$

where $\theta_l = (\pi l / N_x)$ and $\theta_m = (\pi m / N_y)$, and $\tilde{S}_{lm}(z)$ is the discrete Fourier transform of S , which is [cf. RHS of (3)] given by

$$\tilde{S}_{lm} = \sum_{i=0}^{N_x-1} \sum_{j=0}^{N_y-1} S_{ij} \cos\left(\frac{2\pi l x_i}{p_x}\right) \cos\left(\frac{2\pi m y_j}{p_y}\right). \quad (8)$$

The required boundary conditions on $\tilde{V}_{lm}(z)$ are

$$\tilde{V}_{lm}(0) = 0 \quad (9a)$$

$$\begin{cases} \tilde{V}_{lm}(d) = N_x N_y V_a & \text{for } l = 0, m = 0 \\ \tilde{V}_{lm}(d) = 0 & \text{otherwise.} \end{cases} \quad (9b)$$

We begin with an approximate solution for the potential which we denote as $V_{ij}^{(n)}(z)$ where the superscript (n) denotes the n th approximation in our iterative solution. A good choice for the first iteration is the vacuum solution $V_a(z/d)$. We then evaluate $S_{ij}(z)$ by computing the right-hand side of (3), which requires finding the potential minimum of $V_{ij}^{(n)}(z)$. We next compute the Fourier coefficients of \tilde{S}_{lm} using (8), solve (7) for $\tilde{V}_{lm}(z)$ subject to the boundary conditions in (9), and transform the solution to $V_{ij}(z)$ using (6). As in [8], rather than using $\tilde{V}_{lm}(z)$ as the $(n+1)$ -th iteration, we denote this solution as $V_{ij}^{(n+1)}(z)$ and instead define the next iteration of the potential as

$$V_{ij}^{(n+1)}(z) = \alpha V_{ij}^{(n)}(z) + (1 - \alpha) V_{ij}^{(n+1)}(z) \quad (10)$$

where the mixing parameter α is a real number satisfying $0 < \alpha < 1$. The value of α must be obtained empirically, but was typically set in a range from 0.8 to 1. We iterate this algorithm until the solution converges everywhere to 1 part in 10^4 .

III. RESULTS

We use the same diode parameters as [8], setting $V_A = 179.5$ V and $d = 0.381$ mm and apply our 2-1/2-D model to a variety of work function distributions to assess their impact on the Miram curve. First, to demonstrate the space charge shielding effect (and its lack) and resulting current compensation that low work function regions have on their high work function neighbors, we begin with simple arrangements of two work functions: $\phi_1 = 2.0$ eV and $\phi_2 = 2.2$ eV (Fig. 2). We compare the Miram curves resulting from a striped pattern [Fig. 2(a)], first tested in [8], to its natural 2-1/2-D analog: a checkered pattern [Fig. 2(b)], using two different values for the width of each stripe (and of each square side) $s = 53, 265$ μm . For the following tests, unless indicated otherwise, 1024 simulation cells ($N_x = N_y = 32$) were used to model the cathode area, while the vacuum region was discretized into $N_z = 500$ cells. Since the boundaries in x and y are periodic, the entire pattern, as shown in Fig. 2(a) and (b), need not be simulated; a smaller selection can be made such that each “tile” is modeled by 256 (16×16) simulation cells. We see from Fig. 2(c) that for both stripe widths, the current in the checkered case exceeds that of the striped case in the knee region, forming a slightly more rounded knee akin to an experimental Miram curve. Since the current compensation effect occurs primarily at the boundaries between different work functions, it is enhanced by an arrangement that creates more boundaries, i.e., a checkered case. This is made even more apparent in Fig. 2(d), which shows the current density contribution from each work function for the $s = 53$ μm case. As the cathode’s temperature is raised into the transition regime, i.e., the knee of the curve, emission from the 2.0 eV regions in the checkered case is increased, while emission from the 2.2 eV regions is suppressed (relative to the striped case). This effect continues well into the space-charge-limited

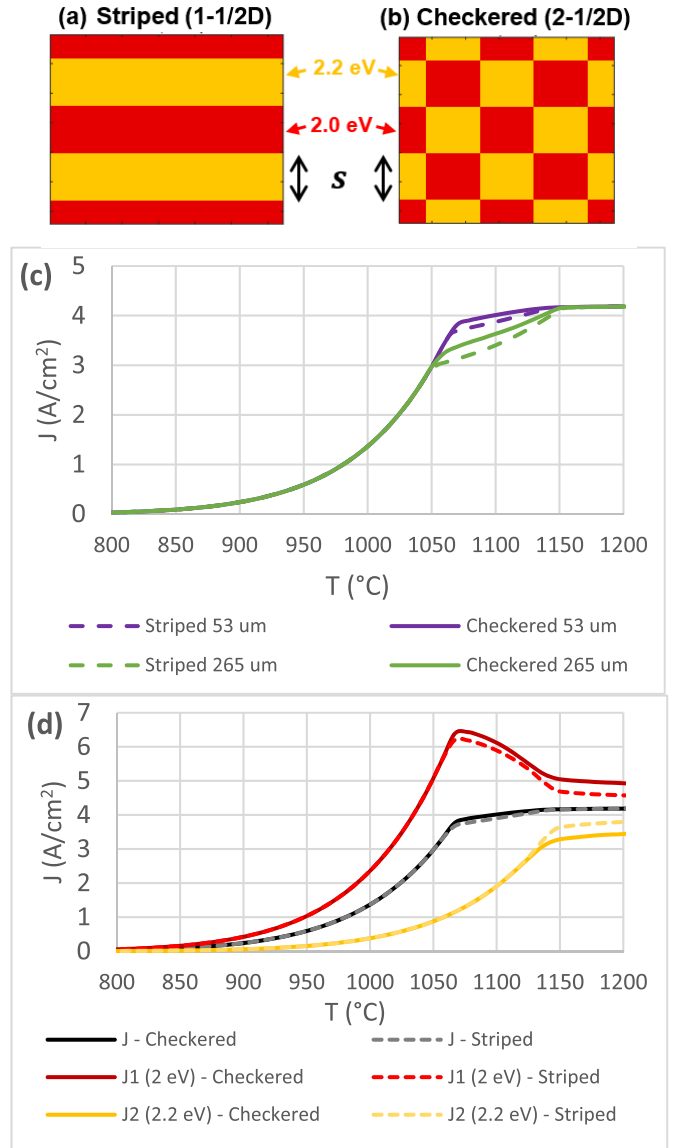


Fig. 2. (a) Striped pattern (1-1/2-D). (b) Checkered pattern (2-1/2-D). (c) Comparison of striped versus checkered arrangements of $\phi_1 = 2.0$ eV and $\phi_2 = 2.2$ eV for two square/stripe widths $s = 53, 265$ μm . (d) Separate current density contributions from ϕ_1 (red curves) and ϕ_2 (yellow curves) for checkered and striped cases, and the total current density (black curves). Here, $s = 53$ μm .

regime, acting in a way to force the overall cathode current density to obey the 1-D Child–Langmuir Law [black curves in Fig. 2(d)].

Next, we replace one in every four 2 eV tiles in the checkered pattern with a nonemitting tile, modeled as having a 10 eV work function [Fig. 3(a)] and labeled “checkered variant.” The resulting Miram curves for $s = 53, 265$ μm compared with the standard checkered pattern are given in Fig. 3(b). First, we note that including a nonemitting region significantly lowers the current in the temperature-limited regime and generally shifts the entire Miram curve to the right. The current is also reduced in the space-charge-limited regime, but this behavior is highly dependent on the tile size s . Smaller tile sizes increase the effective boundary regions where current compensation occurs, thereby sharpening the

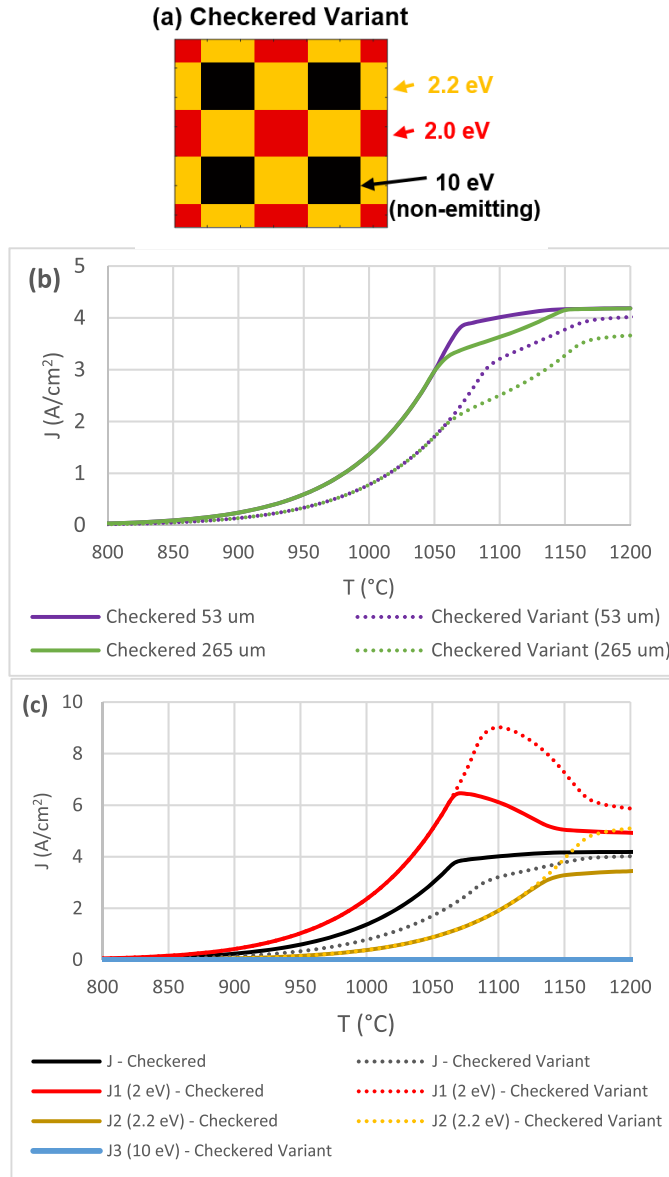


Fig. 3. (a) Checkered variant pattern. (b) Comparison of checkered vs checkered variant patterns for two square widths $s = 53 \mu\text{m}$, $265 \mu\text{m}$. (c) Separate current density contributions from ϕ_1 , ϕ_2 , and nonemitting regions for checkered and checkered variant cases, $s = 53 \mu\text{m}$.

knee and allowing for a higher anode current at lower cathode temperatures. In addition, we observe that at sufficiently high temperatures, both checkered variant cases eventually achieve the 1-D Child–Langmuir current density ($\sim 4.2 \text{ A}/\text{cm}^2$), apparently behaving as if the entire cathode were emitting. However, larger tile sizes significantly delay this process, highlighting the importance of the length scale of different work function regions on the cathode surface in determining the shape of the Miram curve. [This effect of tile size may readily be seen in the hypothetical case where the tile size in Fig. 3(a) is much larger than the AK gap spacing, d .] Fig. 3(c) breaks down the current density contribution from each work function and demonstrates how both the 2 and 2.2 eV regions attempt to compensate current for the nonemitting region, which contributes effectively zero current in the operational temperature range. Under these conditions, the 2.0 eV regions

TABLE I
WORK FUNCTION AREA DISTRIBUTION PERCENTAGES

Work Function (eV)	Experiment [10]	Rand I	Rand II	Rand III
1.61	18.54	17.97	12.89	7.42
1.79	10.32	9.77	8.59	7.42
2.3	10.99	9.38	11.33	11.33
2.31	37.69	43.75	37.50	37.11
10 (non-emitting)	22.46	19.14	29.69	36.72

are capable of supplying a current density over double the 1-D space charge limit. Generally, we observe that the low work function regions contribute to the majority of the anode current, even when they make up a relatively small fraction of the cathode area, as is apparent when we study a more realistic representation of a cathode surface, as follows.

To model a real cathode, we first refer to the work function area distribution, labeled “Experiment [10]” in Table I. The data in this column are the percentages of cathode area occupied by the indicated work function, obtained from electron backscatter diffraction measurements on a tungsten dispenser cathode [10]; the work function values were calculated using density functional theory (DFT) [11]. We once again note the sizeable fraction of nonemitting area that is typical of these cathodes [$\sim 22\%$, on the order of the checkered variant test in Fig. 3(a)] as well as the ability of the cathode to retain the full Child–Langmuir current at sufficiently high temperatures as if the entire cathode were emitting, as we shall also show shortly. We construct the work function distribution pattern in Fig. 4(a) (in which the “Rand I” case is generated by a random number generator to mimic “Experiment [10]” data). A random sequence of 256 work functions is generated in the distributions in Table I. Each tile of work function has an area of $2.5 \mu\text{m} \times 2.5 \mu\text{m}$ and is modeled by four (2×2) simulation cells. Improving the resolution of this grid or testing different randomly generated patterns (with the same work function distribution) did not significantly alter our results. We also constructed two other patterns; in one, the size of the nonemitting area was boosted by 10% [Rand II, Fig. 4(b)], while in the other, it was increased by 15% [Rand III, Fig. 4(c)]. In both, the area of the 1.61-eV regions was reduced to compensate. The resulting Miram curves are given in Fig. 4(d). First, we note how the knee of Rand I appears much more rounded than its 2-1/2-D counterparts by comparing with Fig. 3(b), indicating significant progress toward reproducing an experimental curve. (The smaller tile size used in Fig. 4(d) than in Fig. 3(b) is also a contributing factor, see below.) Increasing the nonemitting area shifts the knee down and to the right, lowering the current density in the knee. In Fig. 4(d), we also include the results of a particle-in-cell simulation of Rand I using the MICHELLE code [12], in which a 20 T magnetic field was applied to restrict all electron motion to be parallel to the z -axis. We observe excellent agreement across the various electron flow regimes: temperature-limited, space-charge-limited, and the transition between them. We additionally remark that the computational time required to solve the anode current at a

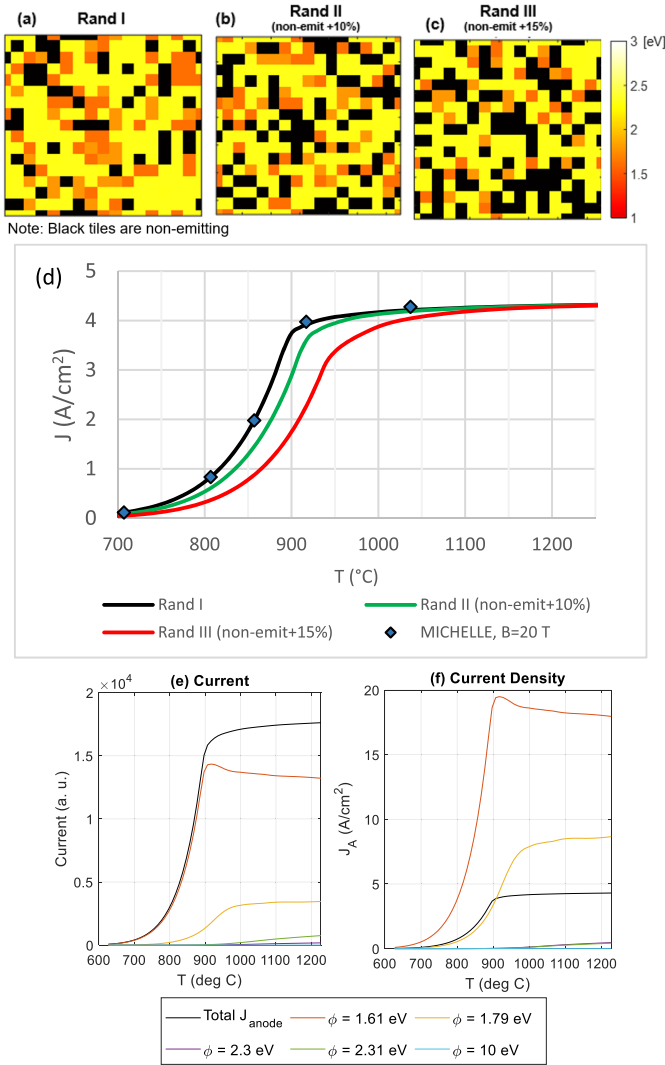


Fig. 4. (a)–(c) Randomly generated work function maps using distributions Rand I, II, and III from Table I. (d) Miram curves of Rand I, II, and III where the nonemitting area is increased by 10% in Rand II and by 15% in Rand III, while the 1.61-eV area is decreased to compensate. (e) Total anode current (black curve) and the anode current from different work function regions (color curves). (f) Anode current density from the total current (black curve) and from different work function regions (color curves). Rand I data are used in (e) and (f).

single temperature is on the order of hours for a MICHELLE simulation, compared with several minutes for the 2-1/2-D code. We stress that Fig. 4(d) shows an extremely rigorous numerical test in that both the 2-1/2-D model and MICHELLE code need to resolve the potential minimum (if one exists) in each of the 256 tiles, including all mutual interactions among the tiles, consistent with the electron orbits that make up the charge distributions within each tile. Yet excellent agreement between these two vastly different numerical calculations was observed in Fig. 4(d).

We show the contribution of current [Fig. 4(e)] and current density [Fig. 4(f)] from each work function region for Rand I. Remarkably, the 1.61 eV region accounts for over 85% of the current contribution in the knee despite only making up $\sim 18\%$ of the actual cathode surface; the current density ascribed to this region is nearly five times the 1-D Child–Langmuir current.

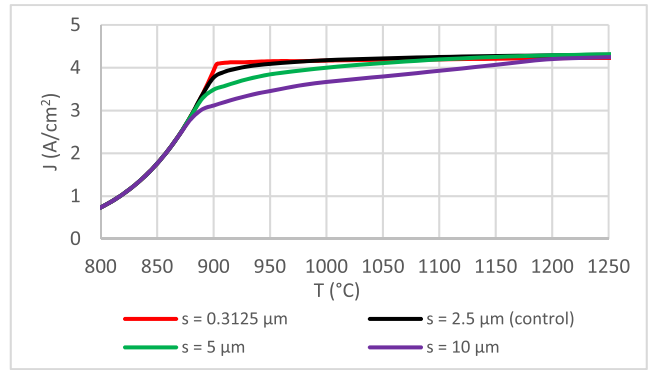


Fig. 5. Effect of varying work function tile size s on shape of Miram curve using work function map Rand I.

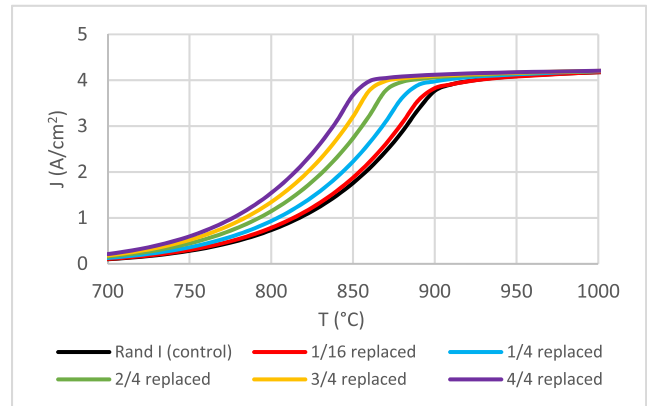


Fig. 6. Simulation of work function map Rand I, with increasing fraction of nonemitting (10 eV) tiles replaced by the highly emitting 1.61-eV tiles.

Next, we use the work function map Rand I [Fig. 4(a)] and vary the width of each work function square from $s = 0.3125$ to 10 μm , plotting the resulting Miram curves in Fig. 5. We observe that as s decreases, the knee grows dramatically sharper. As in the checkered cases (Figs. 2 and 3), smaller tile sizes imply a greater proportion of boundaries relative to surface area. Since the current compensation effect occurs primarily at the boundaries, one would expect that this effect is progressively stronger as the tile size decreases. This phenomenon has some implications on cathode design; if the length scale of work function variations can be reduced, one could obtain a higher anode current density for a lower cathode temperature, thereby improving lifetime and performance [6].

We next perform two additional tests, on the gradual reduction of nonemitting regions (Fig. 6), and on the effects of some local “hot spots,” modeled by very low work functions so that the local emission current density may be excessively high (Fig. 7). In Fig. 6, we replace the nonemitting tiles in Rand I [Fig. 4(a)] with 1.61 eV tiles in increasing fractions: 1/16, 1/4, 1/2, and 1. As one might expect, as the number of low work function tiles increase, the transition temperature between space-charge-limited and temperature-limited flow drops and the knee sharpens as the overall curve shifts to the left. The second test also used Rand I, where we replaced an increasing number of 10 eV work function tiles (which are nonemitting) with 1 eV work function tiles (which are highly emitting).

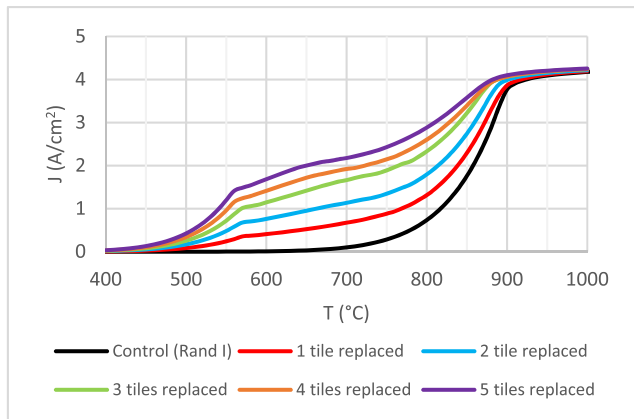


Fig. 7. Simulation of work function map Rand I with increasing number of nonemitting (10 eV) tiles replaced by very highly emitting 1-eV tiles.

The result is shown in Fig. 7. Comparison of the lowest two curves in Fig. 7 shows that just one tile of excessively low work function (of 1 eV) can have a rather significant modification of the Miram curve. The tile size used is $2.5 \mu\text{m} \times 2.5 \mu\text{m}$ in Fig. 7 and in Fig. 4(a). We are tempted to use a highly emitting local spot to represent strong field emission resulting from local cathode surface roughness that is difficult to model, either analytically or in numerical codes. These local hot spots could increase the intrinsic emittance of the generated electron beam [13], [14].

Finally, MICHELLE simulation of Rand I with $B = 0$ shows an increase of anode current by only 2.4 percent at the knee, compared with the MICHELLE run using $B = 20$ T [Fig. 4(d)], and consistent with our previous observation [8] that the electron motion parallel to the cathode surface has little effect on the shape of the Miram curves.

IV. CONCLUSION

This article extends the analytic formulation of Chernin *et al.* [8] to include work function variations along the two dimensions of the surface on a planar thermionic cathode. In addition to being much more realistic in modeling a real cathode surface, it allows a much faster evaluation of various physical effects that could contribute to shape of the Miram curve. We have observed that inclusion of 2-D variations in the work function would yield a Miram curve that is notably more rounded than its 1-D counterpart [8]. From a number of 2-D work function patterns, we recover the 1-D Child–Langmuir limit as if the entire cathode were emitting despite a sizable portion of the area being nonemitting. It remains an intriguing mystery why patch cathode emission, in either the 1-D or 2-D model, conspires to yield an anode current that is governed by the 1-D Child–Langmuir law, as if the entire cathode were emitting. We also illustrate how the low work function regions contribute the most current despite making up a relatively small fraction of the cathode area. In addition, we examine how the size of the patchiness in the work function affects the shape of the Miram curve. In general, smaller length scales yield a sharper knee and, hence, could improve cathode performance. The simple model suggests that a single highly emitting local spot may produce a noticeable modification of the Miram curve.

How these 2-D effects may impact a crossed-field diode [15] remains to be studied.

Our parametric studies of a 2-D work function distribution given in this article imply tremendous difficulty to solve the inverse problem: calculating the work function distribution from experimental Miram curves. Since the emission from a specific location on the cathode surface is highly dependent on the neighboring work function distribution as well as the patchiness length scales, and on whether there are some highly emitting local hot spots, the Miram curve is unlikely to deconvolve into its constituent work function distribution. Our extensive tests using the 2-1/2-D model indicate that PWFD with a narrow work function distribution (~ 0.1 eV [5]), and zero nonemitting regions, will always yield a sharp knee.

ACKNOWLEDGMENT

The views, opinions, and/or findings expressed are those of the authors and should not be interpreted as representing the official views or policies of the Department of Defense or the U.S. Government. Approved for Public Release; Distribution Unlimited.

REFERENCES

- [1] O. W. Richardson, *The Emission of Electricity From Hot Bodies*. London, U. K.: Longmans, Green and Company, 1916.
- [2] T. C. Fry, “The thermionic current between parallel plane electrodes; Velocities of emission distributed according to Maxwell’s law,” *Phys. Rev.*, vol. 17, no. 4, pp. 441–452, Apr. 1921, doi: [10.1103/PhysRev.17.441](https://doi.org/10.1103/PhysRev.17.441).
- [3] I. Langmuir, “The effect of space charge and initial velocities on the potential distribution and thermionic current between parallel plane electrodes,” *Phys. Rev.*, vol. 21, no. 4, pp. 419–435, Apr. 1923, doi: [10.1103/PhysRev.21.419](https://doi.org/10.1103/PhysRev.21.419).
- [4] C. D. Child, “Discharge from hot cao,” *Phys. Rev.*, vol. 32, no. 5, pp. 492–511, May 1911, doi: [10.1103/PhysRevSeriesI.32.492](https://doi.org/10.1103/PhysRevSeriesI.32.492).
- [5] M. J. Cattelino, G. V. Miram, and W. R. Ayers, “A diagnostic technique for evaluation of cathode emission performance and defects in vehicle assembly,” in *IEDM Tech. Dig.*, Dec. 1982, pp. 36–39, doi: [10.1109/IEDM.1982.190205](https://doi.org/10.1109/IEDM.1982.190205).
- [6] A. S. Gilmour, *Klystrons, Traveling Wave Tubes, Magnetrons, Crossed-Field Amplifiers, and Gyrotrons*. Norwood, MA, USA: Artech House, 2011.
- [7] E. A. Adler and R. T. Longo, “Effect of nonuniform work function on space charge limited current,” *J. Appl. Phys.*, vol. 59, no. 4, pp. 1022–1027, Feb. 1986, doi: [10.1063/1.336535](https://doi.org/10.1063/1.336535).
- [8] D. Chernin, Y. Y. Lau, J. J. Petillo, S. Ovtchinnikov, D. Chen, A. Jassem, R. Jaobs, D. Morgan, and J. H. Booske, “Effect of nonuniform emission on miram curves,” *IEEE Trans. Plasma Sci.*, vol. 48, no. 1, pp. 146–155, Jan. 2020, doi: [10.1109/TPS.2019.2959755](https://doi.org/10.1109/TPS.2019.2959755).
- [9] R. J. Umstatt and J. W. Luginsland, “Two-dimensional space-charge-limited emission: Beam-edge characteristics and applications,” *Phys. Rev. Lett.*, vol. 87, no. 14, Sep. 2001, Art. no. 145002, doi: [10.1103/PhysRevLett.87.145002](https://doi.org/10.1103/PhysRevLett.87.145002).
- [10] D. Chen, R. Jacobs, V. Vlahos, D. Morvan, and J. Booske, “Statistical model of non-uniform emission from polycrystalline tungsten cathodes,” in *Proc. Int. Vac. Electron. Conf. (IVEC)*, Apr. 2019, pp. 1–2, doi: [10.1109/IVEC.2019.8745051](https://doi.org/10.1109/IVEC.2019.8745051).
- [11] R. Jacobs, D. Morgan, and J. H. Booske, “Work function and surface stability of tungsten-based thermionic electron emission cathodes,” *Appl. Phys. Lett. Mater.*, vol. 5, no. 11, Nov. 2017, Art. no. 116105.
- [12] J. Petillo, K. Eppley, L. Chernyakova, D. Panagos, J. Burdette, E. Nelson, X. Zhai, N. Dionne, M. Cattelino, J. DeFord, K. Nguyen, B. Held, and B. Levush, “Recent advances in the MICHELLE 2D/3D electron gun and collector modeling code,” in *Proc. 5th IEEE Int. Vac. Electron. Conf.*, Apr. 2004, pp. 322–323, doi: [10.1109/IVELEC.2004.1316341](https://doi.org/10.1109/IVELEC.2004.1316341).
- [13] E. Borie and U. Horcher, “Effect of surface roughness on the velocity spread in electron guns for gyrotrons,” *Int. J. Infr. Millim. Waves*, vol. 18, no. 3, pp. 577–594, Mar. 1997, doi: [10.1007/BF02677996](https://doi.org/10.1007/BF02677996).

- [14] K. L. Jensen, D. A. Shiffler, J. J. Petillo, Z. Pan, and J. W. Luginsland, "Emittance, surface structure, and electron emission," *Phys. Rev. Special Topics—Accel. Beams*, vol. 17, no. 4, Apr. 2014, Art. no. 043402, doi: [10.1103/PhysRevSTAB.17.043402](https://doi.org/10.1103/PhysRevSTAB.17.043402).
- [15] D. Chernin, A. Jassem, and Y. Y. Lau, "Thermal electron flow in a planar crossed-field diode," *IEEE Trans. Plasma Sci.*, vol. 48, no. 9, pp. 3109–3114, Sep. 2020.



Abhijit Jassem received the B.S. degree in nuclear engineering from Purdue University, West Lafayette, IN, USA, in 2016. He is currently pursuing the Ph.D. degree with the University of Michigan's Nuclear Engineering and Radiological Sciences Program. He is working with the Plasma, Pulsed Power, and Microwave Laboratory, University of Michigan.



David Chernin received the Ph.D. degree in applied mathematics from Harvard University, Cambridge, MA, USA, in 1976. Since 1984, he has been with Leidos, Reston, VA, USA, where he is currently a Senior Staff Scientist and its predecessor company SAIC, where he has conducted research on beam-wave interactions and other topics in the physics of particle accelerators and vacuum electron devices.



John J. Petillo (Senior Member, IEEE) received the B.S. degree in electrical engineering from Northeastern University, Boston, MA, USA, in 1980, and the Ph.D. degree in applied plasma physics from the Massachusetts Institute of Technology, Cambridge, MA, USA, in 1986.

His dissertation was on equilibrium and stability analysis of the modified betatron accelerator.

He has been with Leidos Inc., Reston, VA, USA, formerly (Science Applications International Corporation/SAIC), since 1986, first in McLean, VA, USA, and currently in Billerica, MA, USA. Since joining Leidos/SAIC, he has been involved in the research and development of analysis software and analysis and advanced modeling and simulation of RF components, including vacuum electronics, emission physics, accelerator components, microwave devices, ion beam lithography, and ion thrusters. He has been a Lecturer with the U.S. Particle Accelerator School on several occasions in the area of beam and EM-PIC field modeling. He is currently the Director of the Center for Electromagnetic Science, Leidos Innovation Center (LInC), Leidos Inc., and also the Research and Development Manager and an author of the MICHELLE, MASK, AVGUN, and ARGUS Codes.



Y. Y. Lau (Fellow, IEEE) received the B.S., M.S., and Ph.D. degrees in electrical engineering from the Massachusetts Institute of Technology, Cambridge, MA, USA, in 1968, 1970, and 1973, respectively.

He is currently a Professor with the University of Michigan, Ann Arbor, MI, USA, where he is specialized in RF sources, heating, and discharge.

Dr. Lau was elected a Fellow of the American Physical Society in 1986. He was a recipient of the 1999 IEEE Plasma Science and Applications Award and the 2017 IEEE John R. Pierce Award for Excellence in Vacuum Electronics. He served three terms as an Associate Editor for *Physics of Plasmas* from 1994 to 2002.



Aaron Jensen received the B.S. degree in EE with a minor in applied mathematics from the Oregon Institute of Technology, Klamath Falls, OR, USA and the M.S. degree in EE from Stanford University, Stanford, CA, USA.

From 2005 to 2016, he was an Engineering Physicist at SLAC National Accelerator Laboratory, Menlo Park, CA, USA. From 2007 to 2008, he worked at Communication and Power Industries, Palo Alto, CA, USA, and SLAC. While at SLAC, he authored the large signal klystron code AJDISK and was the project manager and engineer for several high efficiency terahertz and sheet beam devices. Since 2016, he has been a Scientist with Leidos, Reston, VA, USA, in Advanced Physics, where he is working on various DoD and DoE programs with an emphasis on high-performance computing, optimization, and code development. He performs electron source design, and designs beam transport/focusing systems, advanced high-current electron accelerator components, and multistage depressed collectors.



Serguei Ovtchinnikov received the B.S. degree in physics and mathematics and the M.S. and Ph.D. degrees in computer science (numerical analysis) from the University of Colorado at Boulder, Boulder, CO, USA, in 1995, 2001, and 2006, respectively.

He is currently a Senior Staff Scientist at Leidos Inc., Billerica, MA, USA. His research interests focus on applications of high-performance computing (HPC) to computational electromagnetics.